JOURNAL OF MATERIALS SCIENCE 22 (1987) 1310–1322

High temperature creep of WC–Co alloys

S. LAY, J. VICENS, F. OSTERSTOCK
Equipe Matériaux-Microstructure, UA 251, ISMRA – Université de Caen, 14032 Caen Cedex, France

The high temperature deformation of tungsten carbide–cobalt composites has been performed in the 1050 to 1350° C temperature range either in compression or in three point bending. The creep behaviour of these materials exhibits a sigmoidal log $\dot{\varepsilon}$–log σ plot with three domains of steady state creep rate possessing a different value of the stress exponent. From recent microscopical and analytical results a microstructural model of the composite is proposed. This model assumes the existence of carbide chains formed of crystals linked with coincidence grain boundaries and takes the number of coincidence grain boundaries into account. It has been used to interpret the creep results. The controlling component of the composite is the tungsten carbide and two deformation processes, grain boundary sliding and intragranular deformation, are the main mechanisms which are involved in the explanation of the creep behaviour. The results of the creep tests are discussed in correlation with transmission electron microscope (TEM) investigations on annealed then deformed samples. TEM microstructural studies of the carbide phase after deformation show an extensive intragranular deformation which has been carefully analysed. Attention has also been paid to the defect structure of grain boundaries.

1. Introduction

Tungsten carbide cobalt alloys have often been seen as a model for two phased materials. This holds for fracture and fracture mechanical behaviour [1–3] as well as for creep [4–6]. The different natures of the carbide and the metallic binder cause one to look for the controlling behaviour of one of them. Furthermore the nature and behaviour of the carbide–carbide grain boundaries have always been a matter of controversy. Depending on the presence or absence of cobalt in these boundaries, the material may be considered as a dispersion of hard particles within a soft matrix, or the existence of a carbide skeleton must be taken into account.

Independently of the lack of technical data and their interest, high temperature creep, with respect to cobalt, may offer a way to answer these questions. Some attempts have already been made [4, 7–11]. Unfortunately, this was done at temperatures either too low or too high. In the first case the difference between dislocation or diffusion creep in the two phases could not be established, and in the second case the temperature was high enough to dissolve the grain boundaries. This may induce artefacts in the interpretation of results obtained at lower temperatures.

It is the aim of this paper to report and discuss creep results obtained at temperatures high enough to make the mechanical response of the two phases quite different without disturbing the nature and behaviour of the carbide–carbide grain boundaries. The temperature range chosen was between 1050 and 1350° C. The cobalt content as well as the mean grain size of the carbide crystals has been varied in a large range.

These conditions have been chosen on the basis of recent microscopical and analytical results. We wanted the two phases to behave quite differently. Furthermore transmission electron microscope (TEM) and high resolution electron microscope (HREM) investigations have shown that there exist general and coincidence carbide–carbide boundaries [12–14]. From the literature it can be expected that they will behave differently at least during creep [15, 16].

Up to now, most of the TEM observations have been made on materials either in the as-sintered state or having been deformed at room temperature [17–19]. Due to the milling and sintering processes, the structure of the defects in the carbide phase is rather complex in the as-sintered state. Plastic deformation of the carbide crystals (single hexagonal structure $a = 0.291\,\text{nm}$; $c = 0.284\,\text{nm}$; $c/a = 0.976$) induces predominantly extended dislocations with a Burgers' vector $\boldsymbol{b} = 1/6\ \langle 1\,1\,\bar{2}\,3\rangle$, which are glissile in the $\{1\,\bar{1}\,0\,0\}$ plane. Only few TEM observations on samples deformed at high temperature have been published [20, 21]. Hibbs *et al.* [21] observed carbide crystals after micro-indentation at 1000° C. They showed extended defects ($b = 1/6\ \langle 1\,1\,\bar{2}\,3\rangle$) and sessile dislocations with a Burgers vector $\boldsymbol{b} = 1/6\ \langle 1\,1\,\bar{2}\,0\rangle$ formed by reaction of partial dislocations.

The results of the creep tests will be discussed in correlation with TEM and STEM investigations on as-sintered or annealed and then deformed samples. Special attention will be paid to the intragranular dislocation structure and to the nature of the grain boundaries.

2. Materials and experimental procedure

The materials were WC–Co composites from the

0022–2461/87 $03.00 + .12

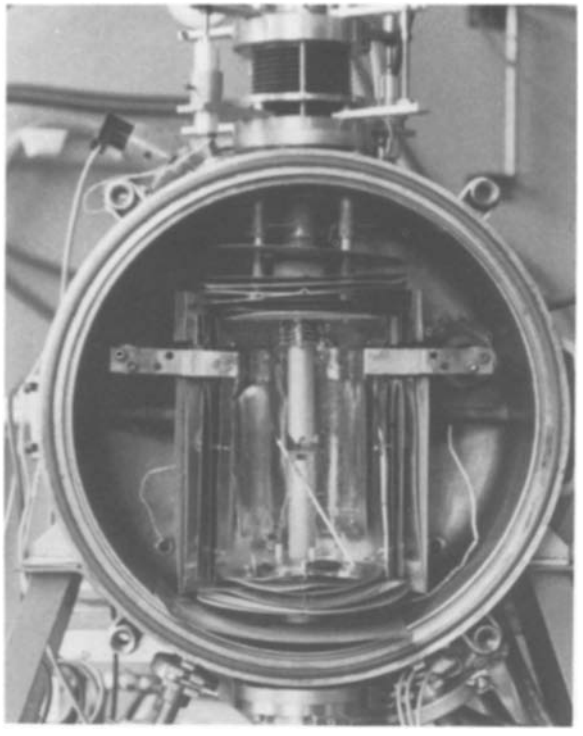

Figure 1 Three point bending set-up in the furnace. Notice the dial gauges and LVDT transducers to measure the displacement. The third thermocouple (Pt–Rh 6–26%) is used to calibrate regularly the W–Rh thermocouples used for temperature measurement and regulation.

Eurotungsten Company (Grenoble, France). They had cobalt volume ratios of 5, 10, 16, 22, 30 and 37%. For each volume ratio, batches having a mean diameter of the carbide crystals, $\bar{D}_{WC}$, of 2.2, 1.1 or 0.7 μm were available.

The creep deformation was performed either in compression (specimen size $4 \times 4 \times 8\,mm^3$) or in three point bending ($2 \times 5 \times 20\,mm^3$). The specimen is positioned between two loading rods in tungsten, 20 mm in diameter. In order to avoid diffusion of cobalt the specimen was isolated from the compression rods by two dense alumina platelets. Indentation creep was not observed.

The experiments were run in vacuum (10^{-5} torr) in a Sesame-type furnace. Compression testing was performed on specimens having a cobalt volume ratio equal to or higher than 16% in volume. For lower ratios we used three point bending. The choice was due to the available facilities (maximum allowed load) and the measurement conditions. In the case of compression a universal Tinius–Olsen, type Locap, testing machine was fitted with a TD A3 constant load programmer. In the case of three point bending, a static set-up, using a lever system, was used. To avoid non-alignment effects, the displacement was measured using two Penny–Gilles inductive transducers. They were placed diametrically on the upper loading road, outside the furnace. They are controlled by two dial strain gauge transducers, also located diametrically on the upper loading road. Fig.1 shows the three point bending loading set up in the furnace.

In compression, true stress, σ, and strain, ε, were calculated. In three point bending, care was taken on the one hand to reach steady state deformation and on the other hand to keep the deviation from linearity valid. A maximum deflection of 1 mm was taken as a limit. We thus used the classical formula of three point bending in the elastic case

$$\varepsilon = \sigma/E = \frac{6eh}{L^2} \quad (1)$$

Derivation with respect to time gives

$$\dot{\varepsilon} = \frac{\partial \varepsilon}{\partial t} = \frac{6e}{L^2}\frac{h}{t} \quad (2)$$

where E is Young's modulus; L is the span (14 mm); e is the thickness of the specimen and h is the deflection of the specimen.

The displacement is measured outside the furnace, but under constant load and steady state creep conditions, it can be assumed to yield the real deflection rate of the sample.

Since the expression for $\dot{\varepsilon}$ in three point bending is only an approximation, these values cannot be directly compared to those obtained for uniaxial compressive loading for all purposes. Creep rate resulting from three point bending always gives overestimates in comparison with compression loading, for example.

For the electron microscope investigations, the samples had been annealed at 1700° C for 4 h before they were subjected to creep deformation. The annealing treatment is intended to eliminate at least partially the defect structure in the carbide crystals. In order to avoid further mechanical stressing, specimens ($5 \times 5 \times 5\,mm^3$) were then spark-cut, deformed at 1450° C under compression and cooled under load. The achieved strain was $\simeq 15\%$. Slices were then spark-cut and thinned (also with spark erosion) to a thickness of 80 μm and a diameter of 3 mm. These discs were finally ion-milled (Ar^+, 6 KeV) for TEM analysis. Jeol 100 CX and 200 CX microscopes were used.

The cobalt concentration at WC–WC grain boundaries and in the carbide grains was determined with X-ray energy dispersive analysis in STEM (Si–Li diode, multichannel analyser SW 9100 Edax). The accelerating voltage was 100 kV. The data were obtained in the spot mode with spatial resolution of 20 nm. The W $L\alpha$ (8.425 KeV) and Co $K\alpha$ (7.065 KeV) rays were used.

3. Microstructural background

The discussions on the microstructure of WC–Co alloys have often stumbled against the question whether a continuous cobalt film exists in the carbide grain boundaries. Several physical analysis methods have been put to work. Viswanadham *et al.* [22] and Lea and B. Roebuck [23] have analysed fracture surfaces using Auger spectroscopy. This method is of too large a scale and suffers two drawbacks. Firstly, it does not take into account the existence of cobalt tearing dimples which are very thin at their bottom and thus contribute to the diminution of the cobalt signal as it is eroded. Secondly, the rupture had been assumed as being essentially intergranular, which is not the case [3, 24]. Thus not all the carbide–carbide grain boundaries have been taken into account.

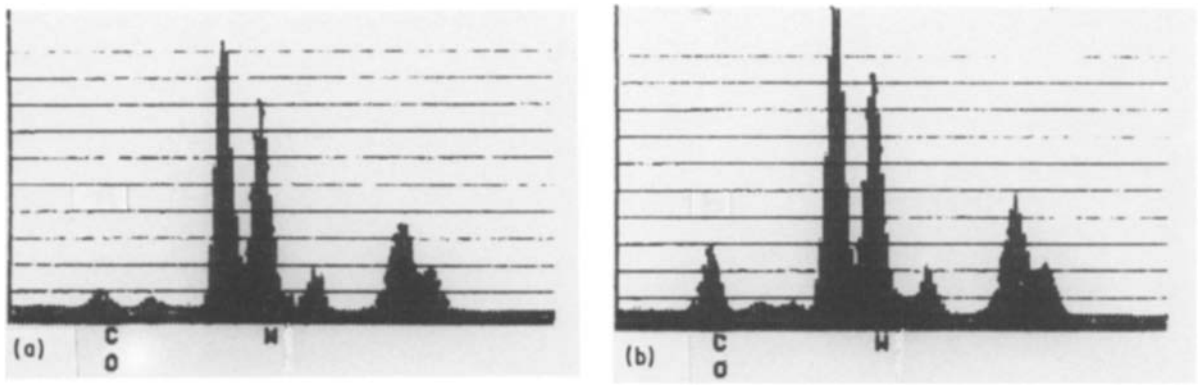

Figure 2 X-ray spectra from (a) a WC grain and (b) a general grain boundary in an as-sintered sample (37 vol % Co).

More recent and accurate investigation methods are HREM observations and STEM analysis. The works of Hagège [12, 13] and Jayaram *et al.* [14] have effectively shown that the carbide–carbide grain boundaries are not all equivalent. An important ratio of grain boundaries are in coincidence.

Concerning the carbide–carbide grain boundaries, current results from the laboratory can be compared with those already published in the literature. Sharma *et al.* [25] made spot analysis with the STEM. They worked with a resolution of 25 nm and found that the Co/W ratio is three times higher in the grain boundaries than in the carbide crystals. The conclusion was the existence of a continuous cobalt layer between the carbide crystals. Friederich [26] used higher resolution (5 nm) and made a profile analysis. He also found cobalt in all the investigated grain boundaries but deduced that it is not sufficient to form a continuous film. Furthermore the cobalt dissolved in the carbide grain was found to segregate.

X-ray energy dispersive analyses of cobalt were made in STEM in the as-sintered samples and also in the annealed deformed specimens. The grain boundaries analysed have been previously orientated.

3.1. Analysis in the as-sintered samples

As a comparison with an annealed and deformed specimen the results obtained in the as-sintered samples (37 vol % Co) are shown in Fig. 2. They correspond to X-ray spectra from a WC grain (Fig. 2a) and a general grain boundary (Fig. 2b). The presence of cobalt is observed in the two spectra. The solubility of cobalt inside the carbide grains is about 3 at %. A cobalt content of 13 at % was found in the general grain boundary. In the case of coincidence grain boundaries there is no marked increase in cobalt content in comparison with that of the adjacent grains; a content of 7.5 at % was effectively found in the $\Sigma = 2$ grain boundary as well as in the adjacent carbide crystals [27]. From these results it was possible to infer a continuous carbide skeleton through coincidence grain boundaries. Other X-ray energy dispersive analyses of cobalt are actually performed in different grain boundaries oriented parallel to the electron beam with a probe stepped along a line perpendicular to the grain boundaries. Other concentration profiles will be published elsewhere.

3.2. Analysis in the annealed then deformed samples

An annealed sample which has been deformed at 1450° C is presented in Fig. 3. This micrograph shows a grain boundary triple point denoted "T" among the three carbide grains denoted 1, 2 and 3, respectively. The different grains have been orientated. The 1–2 grain boundary is a $\Sigma = 2$ coincidence grain boundary and the two others 1–3 and 2–3 are general grain boundaries. The two spectra corresponding to the areas denoted "T" and "M" (Fig. 3) are presented in Fig. 4a and b, respectively. No cobalt was found in the two cases. We conclude that the cobalt phase was evaporated during the annealing treatment. However, as can be seen in Fig. 5, some junctions between grains contain a cobalt pocket. In this example STEM analyses have shown that a cobalt content is observed up to 300 nm from the cobalt phase in carbide grains as well as in grain boundaries. From these results we can consider the annealed and then deformed specimens used in the TEM study as "pure carbide".

3.3. Microstructural model

The above results give good grounds for assuming that the existence of carbide chains formed of crystals linked with coincidence grain boundaries. They thus offer the possibility to sketch a microstructural model very close to the reality. This model shows the material

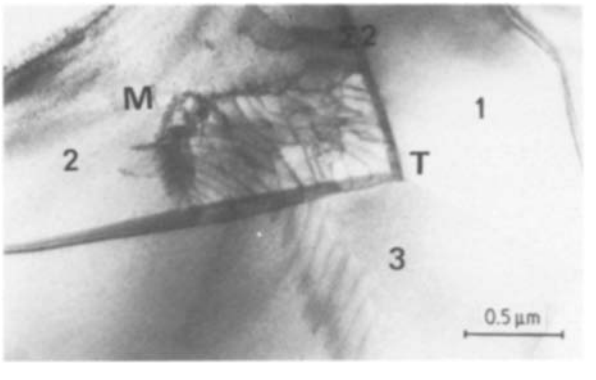

Figure 3 Analysed areas in a sample annealed at 1700° C and then deformed at 1450° C. Original cobalt content was 5 vol % Co. T is the triple junction between the three carbide grains denoted 1, 2 and 3, and M is the area inside the carbide grain numbered 2. The grain boundary between 1 and 2 is in a $\Sigma = 2$ orientation. 1–3 and 2–3 boundaries are general grain boundaries.

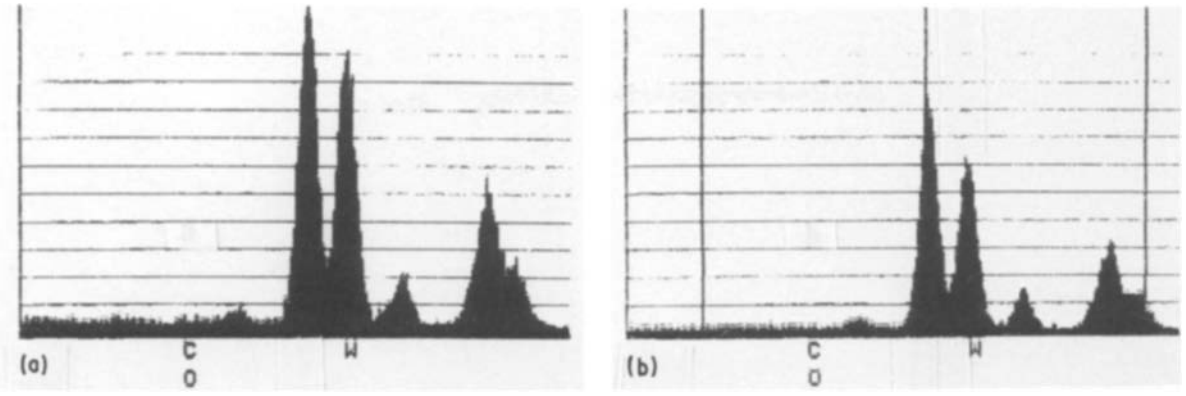

Figure 4 X-ray spectra corresponding to the areas denoted M (Fig. 3a) and T (Fig. 3b).

to be three phased rather than two phased. A schematic representation is given in Fig. 6. We first consider two kinds of carbide grain boundaries: (i) general grain boundaries containing a thin cobalt layer, and (ii) coincidence grain boundaries: they do not contain more cobalt than is dissolved in the carbide crystals.

The three microstructural elements are thus

1. carbide crystal chains linked with coincidence grain boundaries;
2. isolated carbide crystals, having only "general" grain boundaries or interphase boundaries;
3. the cobalt areas, which are schematized as hexagonal black areas in Fig. 6. Their ramifications are not shown in this representation but the model is very close to the reality because the "general" grain boundaries can be seen as cobalt ramifications.

Figs 7 and 8 give some support to the microstructural model. Fig. 7 shows optical micrographs and black and white copies of WC–Co alloys $\bar{D}_{WC}$ = 2.2 μm (Fig. 7a, b, 22 vol % Co; Fig. 7c, d, 37 vol % Co). In contrast to the expected well dispersed two-phased material, it appears that both carbide and cobalt gather into large areas. First comparison with other alloys shows that as the cobalt content increases the areas become larger and gain more branches. The number of cobalt areas does not seem to increase. However, this needs further quantitative investigations. Fig. 8 is a dark field transmission micrograph of the same alloy. Some isolated carbide crystals are present but the left hand part shows linking of carbide crystals in order to form chains. These figures support the existence of carbide crystal aggregates. This has already been suggested in view of fractographic observations. Crack propagation in toughness testing and fracture initiation of unnotched specimens are accompanied by the rupture of these aggregates [3, 24].

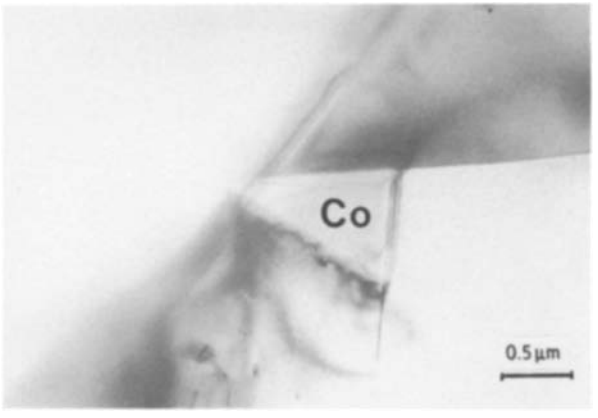

Figure 5 Residual cobalt pocket denoted Co on the micrograph at the junction between four grains.

This model is thus sufficient to interpret the creep results in a first step. It should also be noticed that in the scheme of Fig. 6 the relative number of coincidence grain boundaries is low but changes greatly the aspect of the microstructure. We can thus expect specific creep behaviour. If the carbide phase controls the creep behaviour and if carbide grain boundary sliding occurs, the two kinds of grain boundaries should behave differently and affect the constitutive creep equation.

We will first investigate straightforwardly the creep of WC–Co alloys over a large domain of stress and temperature. The mechanical testing will be followed by TEM investigations on a deformed sample.

4. Results

4.1. Mechanical investigation

High temperature creep rate, $\dot{\varepsilon}$, is usually related to the applied stress, σ, by the relation

$$\dot{\varepsilon} = K\sigma^n \tag{3}$$

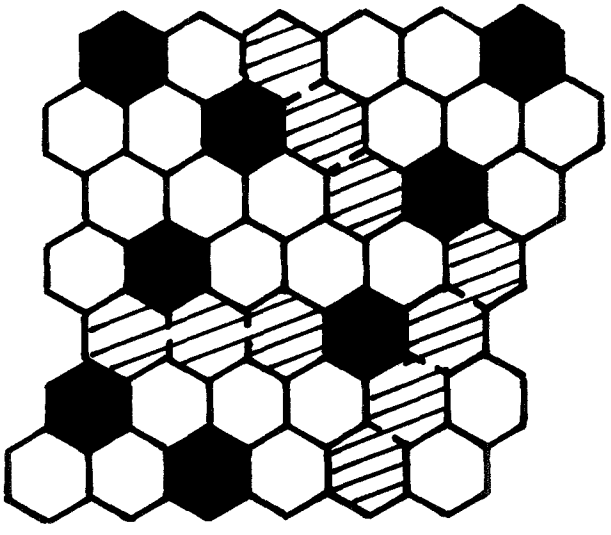

Figure 6 Schematization of the microstructure of WC–Co alloys. Cobalt centres are represented in black. The hatched areas are the carbide chains made of crystals linked by coincidence grain boundaries. The white hexagons are "isolated" carbide crystals separated by general grain boundaries or interphase boundaries.

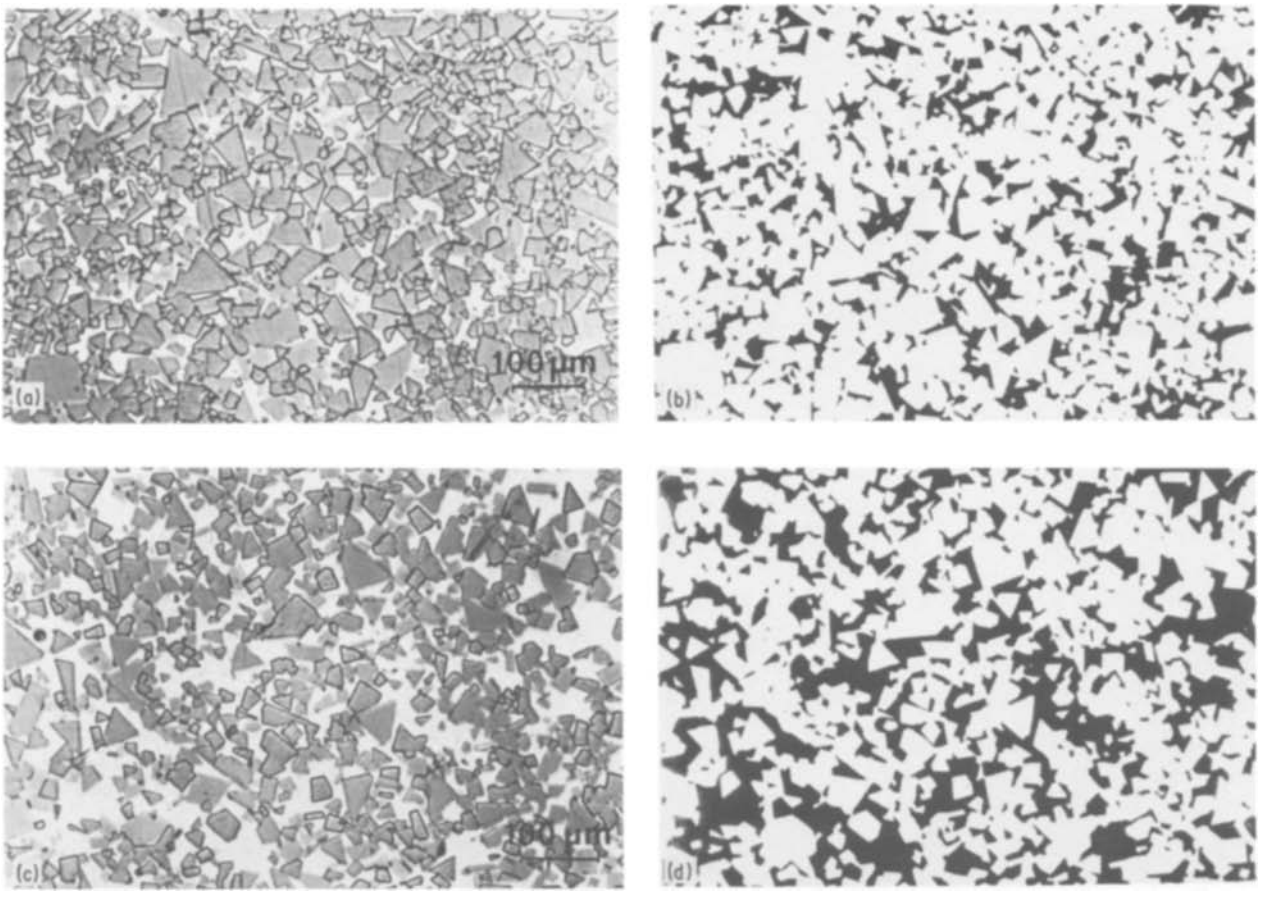

Figure 7 Optical views and corresponding black and white copies of WC–Co alloys with $\bar{D}_{WC} = 2.2\,\mu m$; (a, b) 22 vol % Co; (c, d) 37 vol % Co. On the copies the cobalt is in black and the carbide in white. The contrast is sharper and the distribution of the two phases becomes more sketched.

where n is the stress exponent, and K incorporates effects of temperature and microstructure.

Since there is some automatic discrepancy between compression and three point bending, the effect of microstructure will only be investigated in the former case. Previous creep results on TiC with the same set-up have shown that the stress exponent, n, and the apparent creep activation energy, Q_A, are hardly affected by the method of loading [28]. Both will thus be used in discussing the values of n and Q_A for all the specimens.

To determine the values of n, the results have been plotted as log $\dot{\varepsilon}$ against log σ (Fig. 9). It shows the steady state creep rates obtained with a material, containing 37 vol % cobalt and having a mean grain size of the carbide crystals of $\bar{D}_{WC} = 2.2\,\mu m$, at temperatures between 1000° and 1300° C. A sigmoidal behaviour is observed, the values of the stress exponent, n, being 6–7; 2.7; 4–5 as the applied stress increases. These creep curves will be divided into three domains of steady state creep rates as a function of stress, say Domain I with $n \simeq 6-7$; Domain II with $n = 2.7$ and Domain III with $n \simeq 4-5$.

In the following, only Domain II will be considered because it exhibits high microstructural dependance. This should help one to decide whether the cobalt or the carbide phase is controlling the deformation.

Fig. 10 shows the influence of the cobalt content, (vol %), in Domain II. The sigmoidal shape remains but the slope, i.e. the value of n, increases with the cobalt volume ratio, at a constant value of the mean diameter of the carbide crystals. From Fig. 11 it can be

Figure 8 Dark-field transmission micrograph of an ion-thinned sample (37 vol % Co). The white phase is the cobalt, the dark one is tungsten carbide.

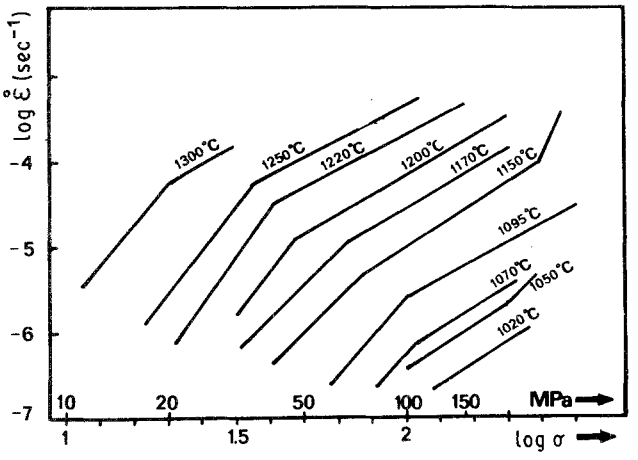

Figure 9 Log $\dot{\varepsilon}$ against log σ plot showing the sigmoidal shape of the creep rate as a function of stress for various temperatures. The alloy contains 37 vol % Co; the mean diameter of the carbide crystals is 2.2 μm.

seen that the cobalt volume ratio is the only microstructural parameter which influences the value of the stress exponent. As a general trend, creep rate increases with cobalt volume ratio at constant values of applied stress and mean diameter of the carbide crystals. Furthermore, a decrease in grain size induces an increase in strain rate (Fig. 11). The influence of cobalt content and carbide crystal size in Domain II could only be determined in a limited domain of applied stress. The results are summarized in Fig. 12; independently of cobalt volume ratio, the dependance of creep rate on the mean grain size of the carbide crystal can be described as

$$\dot{\varepsilon} = A \cdot \bar{D}_{WC}^{-2} \cdot \sigma^n \exp(-Q_A/RT) \qquad (4)$$

where Q_A is the apparent activation energy of the creep process.

As a comparison, one can observe that in Domain I the influence of the microstructural parameters is almost narrow. Due to the high strain rates which were attained and the high load which would have been needed, the high stress–high exponent domain has not been investigated.

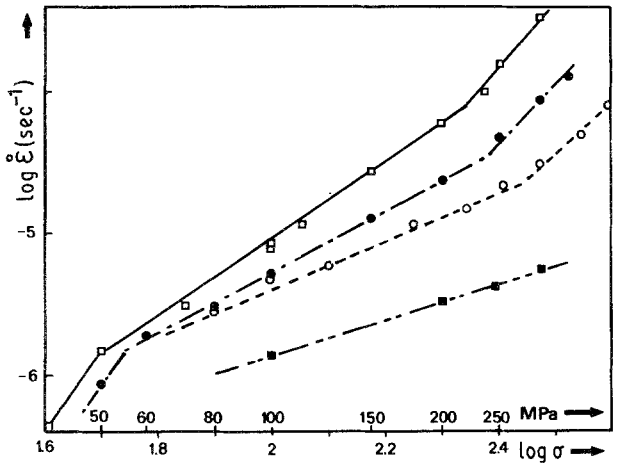

Figure 10 Influence of cobalt content and stress on the creep rate in Domain II. The stress exponent increases with cobalt volume ratio. θ = 1150° C; $\bar{D}_{WC}$ = 2.2 μm. □, 37 vol % Co, M = 2.70; ● 30 vol % Co, M = 2.10; ○, 22 vol % Co, M = 1.65; ■, 16 vol % Co, M = 1.25.

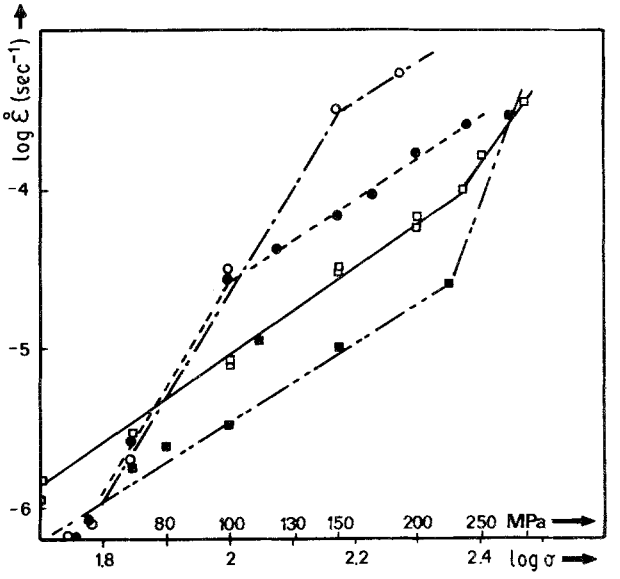

Figure 11 Influence of the mean diameter of the carbide crystals on the creep rate in Domain II. The stress exponent remains constant but the creep rate increases with decreasing crystal size. 37 vol % Co; θ = 1150° C. $\bar{D}_{WC}$; ■ 6.5; □, 2.2; ●, 1.1; ○ 0.7.

The results from compression testing showed that the stress exponent is solely dependent on the cobalt volume ratio. The measurements on the alloys with low cobalt volume ratio have thus been undertaken in order to verify that it tends continuously towards some value and that the activation energy remains constant. The results are shown in Fig. 13; the stress exponent, n, tends to 1 as the cobalt volumic ratio tends to 0.

Fig. 14 shows that the apparent creep activation energy is quite independent of the applied stress, i.e. whether it describes Domain I, II or III. Furthermore, the plots in Fig. 15 show that it is also independent of cobalt volume ratio and of the method of loading; the activation energy of the creep process has a constant value of $Q_A \simeq 540$–$580\,\mathrm{kJ\,mol^{-1}}$ or 5 to 5.40 eV.

4.2. TEM observations

TEM observations of annealed specimens which have been deformed at 1450° C reveal an extensive and inhomogeneous deformation. The most characteristic

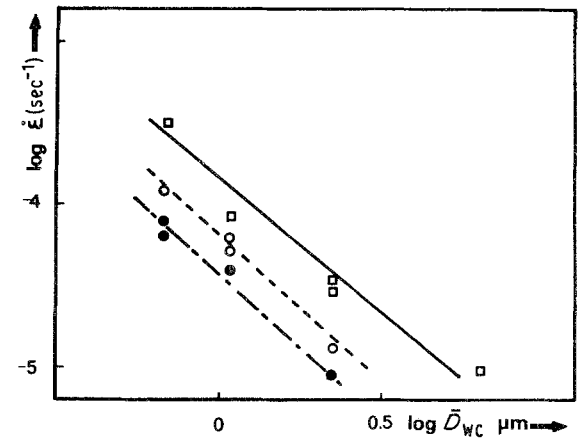

Figure 12 Plot of the steady state creep rate as a function of the mean diameter of the carbide crystal for various cobalt volume ratios at a stress of 150 MPa. θ = 1150° C; σ = 150 MPa. Vol % Co: □, 37; ○, 30; ●, 22.

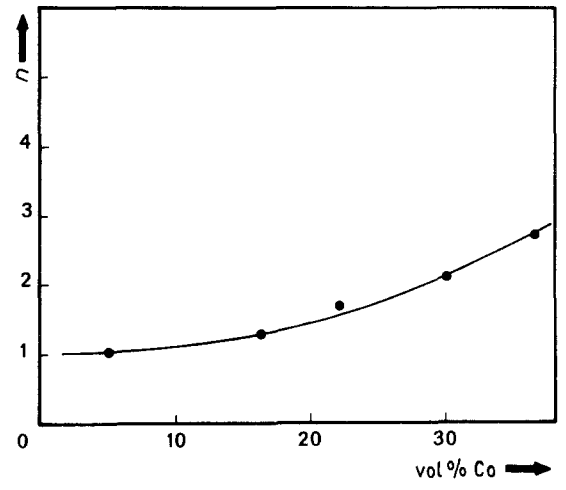

Figure 13 Variation of the stress exponent with cobalt volume ratio. As vol % Co tends towards 0, n tends towards 1.

feature is the formation of subgrain boundaries. Intergranular deformation is also depicted. The defect structure of a large number of grain boundaries has been studied.

4.2.1. Intragranular deformation and dislocation structure

Interactions between dislocations and subgrain boundaries are often observed; an example is shown in Fig. 16. A detailed analysis of such an interaction will be described later. A large number of subgrain boundaries are well defined and an example is presented in Fig. 17. Their characterization has already been performed [29]. Table I gives the main geometrical elements. They have a rotation angle close to 1° and are formed with one family of dislocations. From Table I it appears that three main types of pure tilt subgrain boundaries can be formed in WC. They have been classified according to the Burgers' vectors of their dislocations: $\langle 0\,0\,0\,1\rangle$ Type I; $1/3\,\langle 1\,1\,\bar{2}\,0\rangle$ Type II; $1/3\,\langle 1\,1\,\bar{2}\,3\rangle$ Type III.

The subgrain boundaries with $\boldsymbol{b} = \langle 0\,0\,0\,1\rangle$ (Type I) are formed with dislocation segments located in the $\{1\,0\,\bar{1}\,0\}$ glide planes of WC. These subgrain boundaries can easily migrate under stress by glide of their individual dislocations. Consequently they are more seldom observed. Geometrical considerations show that the two types of subgrain boundaries (Types I and II) can result from dislocation sources in the $\{0\,0\,0\,1\}$ and $\{1\,0\,\bar{1}\,0\}$ planes and climb processes.

The pure tilt subgrain boundaries with $\boldsymbol{b} = 1/3\,\langle 1\,1\,\bar{2}\,3\rangle$ possess a long range stress field when their boundary plane is parallel to the $\{0\,0\,0\,1\}$ planes. For these cases, only the component of the Burgers' vector perpendicular to the boundary plane gives rise to a rotation. This component is $\boldsymbol{b}' = [0\,0\,0\,1]$. The other component $\boldsymbol{b}'' = 1/3\,[1\,1\,\bar{2}\,0]$ lies in the boundary plane and gives rise to a long range stress field [30].

Interactions between dislocations and subgrain boundaries are often observed (Fig. 16) especially when they are of Type III. An example is analysed in Fig. 18. The subgrain boundary shown in two different orientations has a boundary plane parallel to the $(0\,0\,0\,1)$ plane. It consists of a family of $1/3\,[\bar{2}\,1\,1\,\bar{3}]$ dislocations denoted 1 in Figure 18a. Two $1/3\,[\bar{1}\,2\,\bar{1}\,3]$ dislocations (denoted 2) have a screw character. They are inserted partly in the subgrain boundary and change their dislocation line orientations. This insertion can be explained by a cross slip mechanism from the $(1\,0\,\bar{1}\,0)$ glide plane to the $(2\,\bar{1}\,\bar{1}\,\bar{1})$ plane. All the geometrical elements are plotted on the stereographic projection of Fig. 18c.

No dissociated dislocations have been observed in the subgrains (Type III). Their formation needs a climb process and therefore a recombination process if they are dissociated. Some isolated dissociated dislocations with Burgers' vector of the type $1/6\,\langle 1\,1\,\bar{2}\,3\rangle$ have been found in carbide grains. They are frequently observed after deformation at room temperature as a result of the activation of $\{1\,0\,\bar{1}\,0\}$ glide planes.

However, after high temperature deformation the $1/6\,\langle 1\,1\,\bar{2}\,3\rangle$ dislocations do recombine over a part of their line due to the climb process. An example is presented in Fig. 19. It can be seen that a $1/3\,\langle 1\,1\,\bar{2}\,3\rangle$ dislocation is dissociated over the part denoted "L_1" on the micrograph; the two $1/6\,\langle 1\,1\,\bar{2}\,3\rangle$ partial dislocations are partly recombinated over part "L_2" from

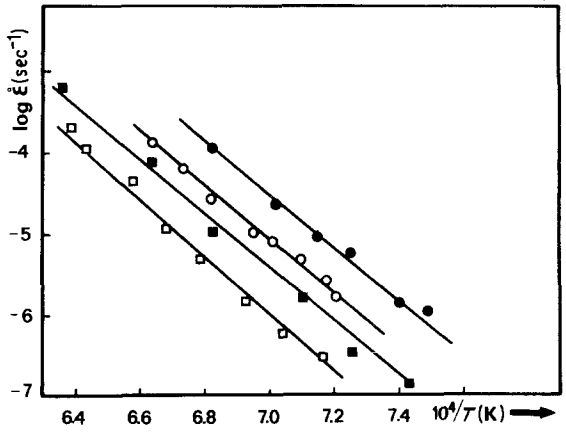

Figure 14 Arrhenius plot of the steady state creep rate for various values of the applied stress (compression). The stress values cover Domains I, II and III for the alloy. 2.2 μm; 37 vol % Co. □, 50; ■, 70; ○, 100; ●, 200 MPa.

TABLE I Geometrical elements of subgrain boundaries in WC after high temperature deformation

Burgers' vector of dislocations	Direction of dislocation lines	Subgrain boundary plane
$[0\,0\,0\,1]$	$[1\,1\,\bar{2}\,0]$	$(0\,0\,0\,1)$
$[0\,0\,0\,1]$	$[1\,1\,\bar{2}\,0]$	$(0\,0\,0\,1)$
$[0\,0\,0\,1]$	$[3\,\bar{1}\,\bar{2}\,0]$	$(0\,0\,0\,1)$
$1/3\,[1\,\bar{2}\,1\,0]$	$[4\,1\,\bar{5}\,3]$	$(1\,\bar{3}\,2\,0)$
$1/3\,[1\,\bar{2}\,1\,0]$	$[1\,0\,\bar{1}\,1]$	$(1\,\bar{3}\,2\,0)$
$1/3\,[1\,\bar{2}\,1\,0]$	$[1\,0\,\bar{1}\,1]$	$(1\,\bar{3}\,2\,0)$
$1/3\,[1\,\bar{2}\,1\,0]$	$[2\,0\,\bar{2}\,3]$	$(1\,\bar{2}\,1\,0)$
$1/3\,[1\,\bar{2}\,1\,0]$	$[1\,0\,\bar{1}\,0]$	$(1\,\bar{2}\,1\,0)$
$1/3\,[1\,\bar{2}\,1\,0]$	$[4\,\bar{2}\,\bar{2}\,3]$	$(0\,1\,\bar{1}\,0)$
$1/3\,[1\,1\,\bar{2}\,3]$	$[0\,1\,\bar{1}\,0]$	$(0\,0\,0\,1)$
$1/3\,[\bar{1}\,2\,\bar{1}\,3]$	$[0\,1\,\bar{1}\,0]$	$(0\,0\,0\,1)$
$1/3\,[\bar{1}\,2\,\bar{1}\,3]$	$[0\,1\,\bar{1}\,0]$	$(0\,0\,0\,1)$
$1/3\,[\bar{1}\,2\,\bar{1}\,3]$	$[0\,1\,\bar{1}\,0]$	$(0\,0\,0\,1)$
$1/3\,[\bar{2}\,1\,1\,\bar{3}]$	$[0\,1\,\bar{1}\,0]$	$(0\,0\,0\,1)$
$1/3\,[\bar{2}\,1\,1\,3]$	$[2\,0\,\bar{2}\,3]$	$(\bar{2}\,1\,1\,2)$
$1/3\,[\bar{2}\,1\,1\,3]$	$[2\,0\,\bar{2}\,3]$	$(\bar{3}\,2\,1\,2)$
$1/3\,[\bar{1}\,2\,1\,3]$	$[1\,0\,\bar{1}\,0]$	$(1\,\bar{2}\,1\,2)$

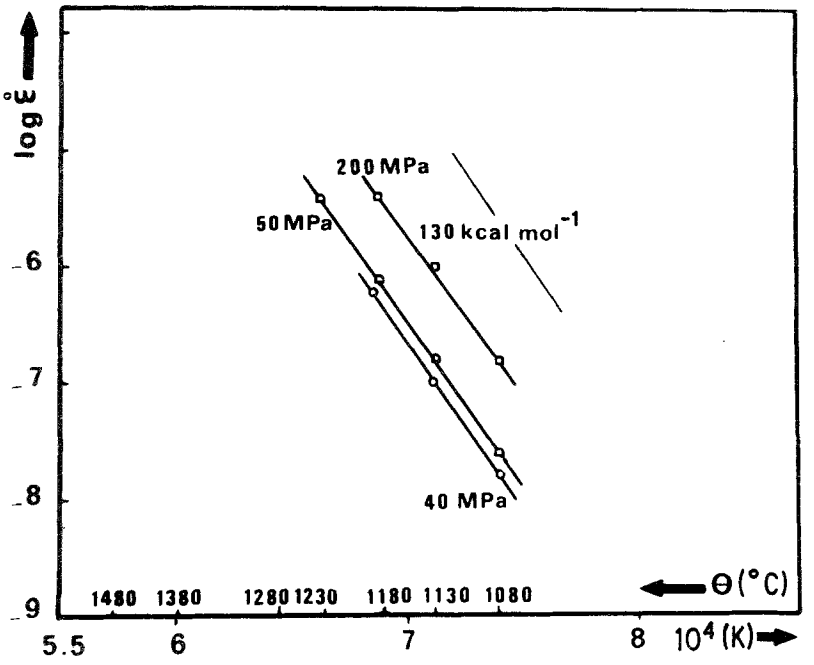

Figure 15 Arrhenius plot for the three point bending results and comparison with a plot from compression measurement. The same activation energy was obtained for the three materials (□, A103, ⌓, H03T, ○, A2003) at the same cobalt volume ratio (5 vol % Co). These three alloys have a different mean carbide grain size: $\bar{D}_{WC}$ = 0.7 μm (A2003); 0.8 μm (H03T); 2.2 μm (A103). The alloy tested in compression (A2025) has a cobalt volume ratio 37 vol % Co and a mean carbide grain size $\bar{D}_{WC}$ = 0.7 μm.

the point 0. Some local dissociations can also be seen in "L_2" and have been arrowed on the micrograph.

4.2.2. Intergranular deformation

Systematic observations of grain boundaries have been performed after high temperature deformation on coincidence and general grain boundaries. It appears that few grain boundaries contain dislocations. Grain boundary dislocations are only observed in coincidence grain boundaries, some of which are listed in Table II. Frequent interactions exist between subgrain boundaries and grain boundaries, they are also indicated in Table II.

An example of dislocations in a Σ = 2 coincidence grain boundary is presented in Fig. 20 where four grains denoted 1, 2, 3 and 4 are imaged. A characterization of their orientation has been performed and Σ = 2 relationships have been found between grains 1 and 2, and grains 2 and 3. Interactions between subgrains and grain boundaries can also be seen. Only dislocations in the Σ = 2 grain boundary between grains 1 and 2 have been analysed. They have a 1/3 $[\bar{1}\,2\,\bar{1}\,3]$ Burgers' vector which has a component out of the $(1\,\bar{1}\,0\,0)$ boundary plane. Therefore the movement of these dislocations involves glide and climb processes.

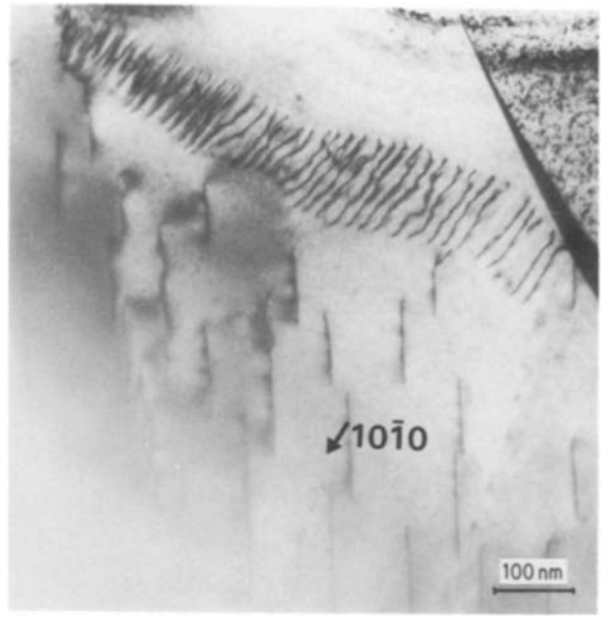

Figure 16 Interaction between dislocations and a subgrain boundary inside a carbide grain observed in an annealed then deformed sample.

5. Discussion

From the experimental results we can conclude that the carbide phase controls the creep deformation of the WC–Co alloys.

The values of the stresses needed to deform the material are very high. Comparison with known creep data of cobalt [31, 32] or with a TiC–Co particular composite (50 vol % Co) do not account for the resulting low creep rates if the deformation were controlled by the cobalt. At the same temperature and stress the TiC–Co alloy has a creep rate over three orders of magnitude higher than the WC–Co alloy with 37 vol % Co [6].

Furthermore, the value of the creep activation energy (Q_A = 540–580 kJ mol^{-1}) is very close to the activation energy of diffusion of W in WC. In the

TABLE II Main features of the analysed grain boundaries in high temperature deformed WC

Σ	Boundary plane	Number of subgrain boundaries intersecting the grain boundary	Intergranular dislocations
2	$(1\,\bar{1}\,0\,0)^{1,2}$	0	observed
> 50	$(0\,0\,0\,1)^{1,2}$	0	–
2	$(\bar{1}\,\bar{4}\,5\,2)^1(\bar{1}\,2\,\bar{1}\,2)^2$	1	observed
4	$(0\,0\,0\,1)^1(3\,0\,\bar{3}\,2)^2$	1	–
2	$(1\,\bar{1}\,0\,0)^{1,2}$	1	observed
2	$(1\,\bar{1}\,0\,0)^{1,2}$	2	observed
2	$(1\,\bar{1}\,0\,0)^{1,2}$	0	–
2	$(1\,\bar{1}\,0\,0)^{1,2}$	1	observed
13a	$(0\,0\,0\,1)^{1,2}$	0	–
13a	$(0\,0\,0\,1)^{1,2}$	1	observed
2	$(1\,\bar{1}\,0\,0)^{1,2}$	0	observed

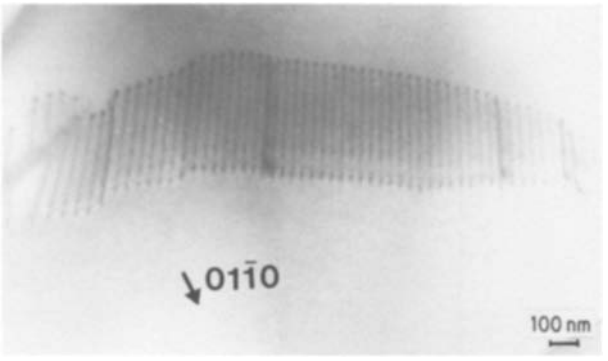

Figure 17 A well-defined subgrain boundary.

range 2100–2400° C a value of 580 kJ mol^{-1} had been measured [33]. The creep activation energy is also higher than the self-diffusion energy of cobalt (252 kJ mol^{-1}). It remains constant over the three domains of creep. This indicates also that a unique elementary intragranular mechanism is acting even if several creep mechanisms are operating simultaneously as can be expected in Domain II. The TEM investigations have shown that dislocation climb is one of the elementary mechanism. Since climb is controlled by the metallic (largest) component, this would be in accordance with the diffusion activation energy of W in WC and the temperature range we have investigated.

The activation energy we have measured is higher than those already published by other authors. The latter are scattered over a large range, varying from 45 to 400 kJ mol^{-1} [5, 7–11]. Generally a rapid overview shows, that the values of the reported activation energies increase with increasing testing temperature. This seems to have several causes. Below 1000° C the deformability of the alloy is function of both the testing temperature and the cobalt volume ratio. It is thus quite possible that the steady state creep has not been reached in all the cases. Only Williams [5] measured activation energies at temperatures slightly higher than our testing range. They obtained a maximum value of 400 kJ mol^{-1}. However, they used the variation of the yield stress with temperature and did not take into account the influence of the stress exponent, n, in deriving $\ln\sigma$ against $1/T$. If $n > 1$, this yields an underestimate of the activation energy.

In Fig. 21 we compare our results with some of the data found in the literature. Apart from the results of Mal [9], a rather good correlation is found with other authors.

Some previously published [20] TEM observations on WC–Co samples, deformed between 1100 and 1400° C, have shown a heterogenous dislocation density within the WC grains but no detailed analyses have been reported. It has only been suggested that dislocation climb would be inhibited by the presence of extended nodes in observed dislocation networks. Our TEM investigations were performed in previously annealed specimens deformed at 1450° C and we have found a heterogeneous deformation in carbide grains. Detailed analysis of the dislocation structure shows that most of the 1/3 $\langle 1\,1\,\bar{2}\,3\rangle$ dislocations are not dissociated. They formed well defined subgrain boundaries. Some observations on partly recombinated 1/6 $\langle 1\,1\,\bar{2}\,3\rangle$ dislocations suggest that climb of such dislocations involves a dislocation recombination. Interaction between dislocations and these subgrain boundaries have also made evidence of a possible cross slip mechanism for 1/3 $\langle 1\,1\,\bar{2}\,3\rangle$ dislocations. Other subgrain boundaries formed with $\langle 0\,0\,0\,1\rangle$ and 1/3 $\langle 1\,1\,\bar{2}\,0\rangle$ perfect dislocations are also observed. These results clearly show that dislocation climb is an important mechanism in the intragranular deformation of carbide crystals at high temperature.

As shown before, dislocations are frequently observed in coincidence grain boundaries. On the other hand, no dislocations are imaged in general grain boundaries. Only qualitative observations on grain boundary dislocations have been reported here. Intergranular dislocations studies are in progress and will be published elsewhere.

These observations are in agreement with experiments on grain boundary sliding correlated with the

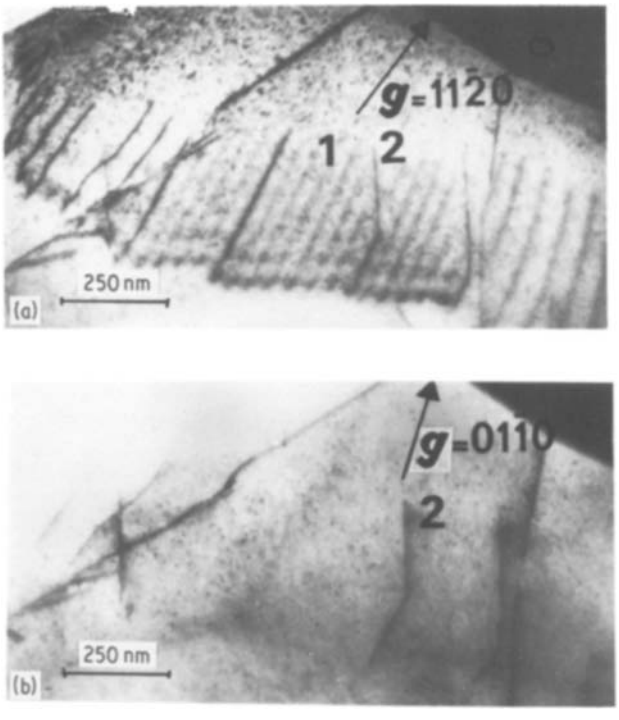

Figure 18 (a) Subgrain boundary formed with dislocations 1 ($\boldsymbol{b}_1$ = 1/3 $[\bar{2}\,1\,1\,\bar{3}]$). Dislocations denoted 2 have a 1/3 $[\bar{1}\,2\,\bar{1}\,3]$ Burgers' vector. They are imaged with $\boldsymbol{g} = 1\,1\,\bar{2}\,0$. (b) Dislocations 1 are out of contrast with $\boldsymbol{g} = 0\,1\,\bar{1}\,0$. (c) Stereographic projection showing the different geometrical elements of the subgrain boundary.

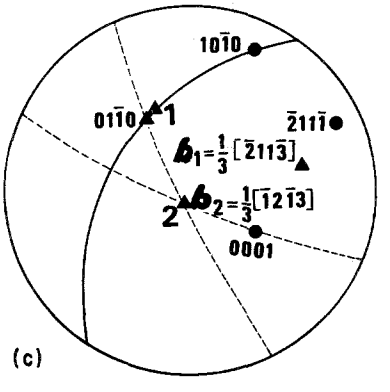

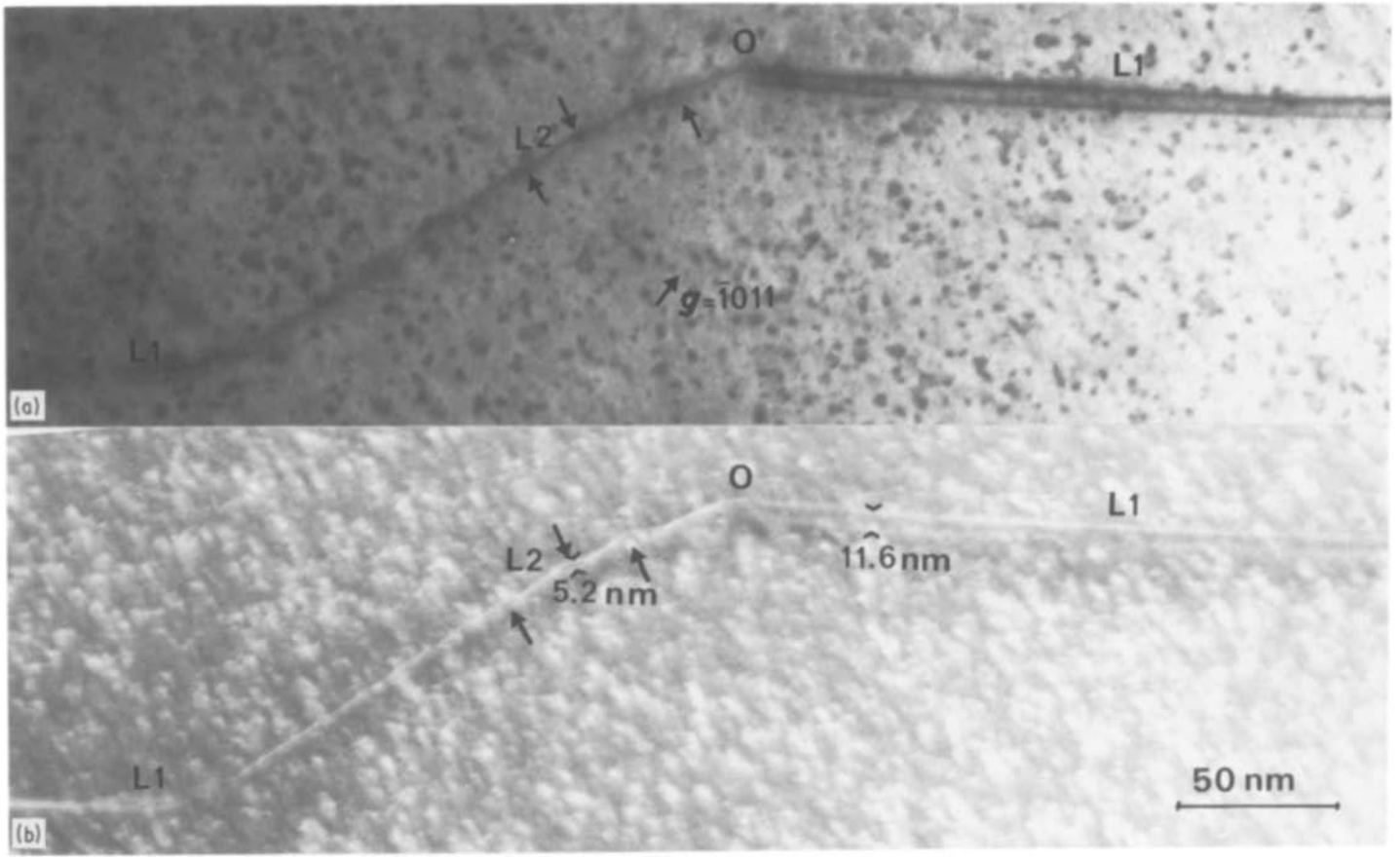

Figure 19 Example of a recombination process during climbing of 1/6 ⟨1 1 $\bar{2}$ 3⟩ partial dislocations. (a) The dislocation is a bright field image with $\boldsymbol{g} = \bar{1}\,0\,1\,1$. On part L_1, the dislocation is dissociated and partly recombinated in the part L_2 from the point denoted 0. (b) Weak beam image with the same $\boldsymbol{g}$. The dissociation width is 11.6 nm in part L_1 and 5.2 nm for the local dissociations in part L_2 (arrowed).

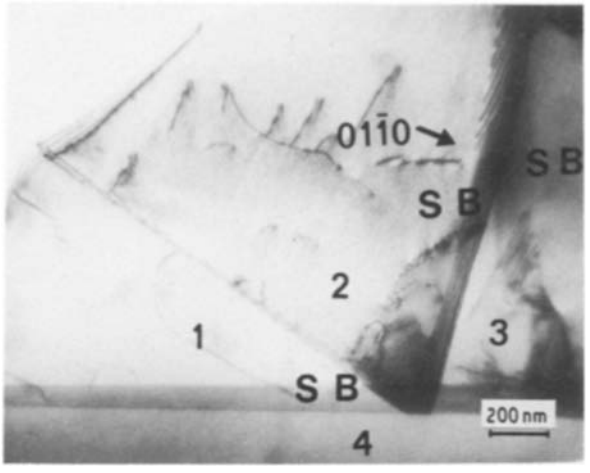

Figure 20 Example of intergranular dislocations in (1–2) and (2–3) $\Sigma = 2$ grain boundaries. Interactions with subgrain boundaries denoted SB are indicated.

presence of dislocations in grain boundaries [15, 34]. They can be explained by a dislocation model of sliding with absorption of lattice dislocations in the grain boundaries. The absorption of lattice dislocations needs their dissociation in the DSC lattice. The grain boundary sliding is explained by the movement of these intergranular dislocations in the grain boundary.

According to this model, the absorption of lattice dislocations is more difficult in coincidence grain boundaries than in general grain boundaries where small Burgers' vectors are involved. Moreover glide and climb processes are necessary for the dislocation movement in the grain boundary. It is known that grain boundary diffusion is more difficult in coincidence grain boundaries than in general grain boundaries. In consequence, easy sliding takes place in general grain boundaries, whereas, on the contrary, a rapid slide hardening of the coincidence grain boundaries occurs. This explains the number of dislocations observed in coincidence grain boundaries and the frequent interactions between subgrain boundaries and coincidence grain boundaries.

The creep data can be summarized by the schematic draft in Fig. 22. The three domains of steady state creep are represented. The influence of the main experimental parameters (temperature and microstructure) is also given.

The sigmoidal shape of the curve, i.e. the presence of several stress exponents, can be described by the occurrence of both grain boundary sliding and intragranular creep deformation. This can be done within the scope of a transition from relaxed to unrelaxed grain boundary sliding as it has been proposed several times [35, 36]. In these models the transition takes place in an almost narrow stress domain. This domain would correspond to our Domain II which is, however, more extended. Furthermore the stress exponent in this domain is a function of the cobalt volume fraction. From scanning and transmission electron microscopic observations we conclude that grain boundary sliding exists (see Fig. 23), that the general grain boundaries act as perfect dislocation sinks and that the coincidence grain boundaries harden very quickly and hardly slide (in respect to the general grain boundaries). With these assumptions the possible mechanisms for the three observed domains are as follows.

1. Domain I: the general grain boundaries would glide easily but they need lattice deformation of the carbide crystals to be accommodated. Thus lattice deformation of the carbide phase is the controlling factor.

2. Domain II: this is a special case of creep of two phases, the isolated crystals having only general grain boundaries and the carbide crystal chains or aggregates linked by coincidence grain boundaries. The former are subject to grain boundary sliding with a stress exponent of $n = 1$. For reasons of deformation compatibility the aggregates must deform at the same macroscopic rate. Since the coincidence grain boundaries hardly slide, the aggregates will creep through an intragranular deformation process with a stress exponent $n = 4$–5. In these conditions, Domain II is a mixture of simultaneous grain boundary sliding creep and intragranular power-law creep.

3. Domain III: the lattice deformation rate of the carbide crystals is much higher than that due to grain boundary sliding, and is once more the controlling factor of the creep rate.

Chen and Argon and others have investigated the creep on two-phased materials using the self-consistent theory for polycrystals [36–40]. They concluded that

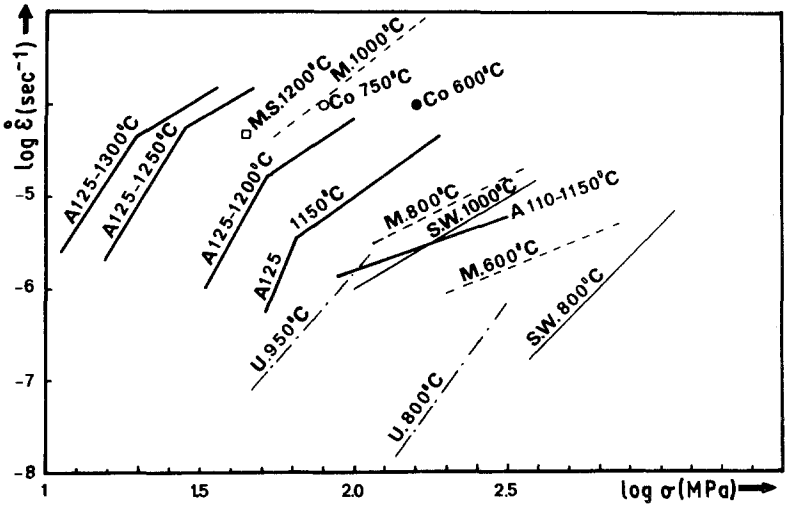

Figure 21 Comparison of the creep rates of one of the WC–Co alloys ($\bar{D}_{WC} = 2.2\,\mu m$; 37 vol % Co) with data from the literature. M, Mal [9], M. S., Murray and Smith [41]; S. W., Smith and Wood [4]; U, Ueda *et al.* [11].

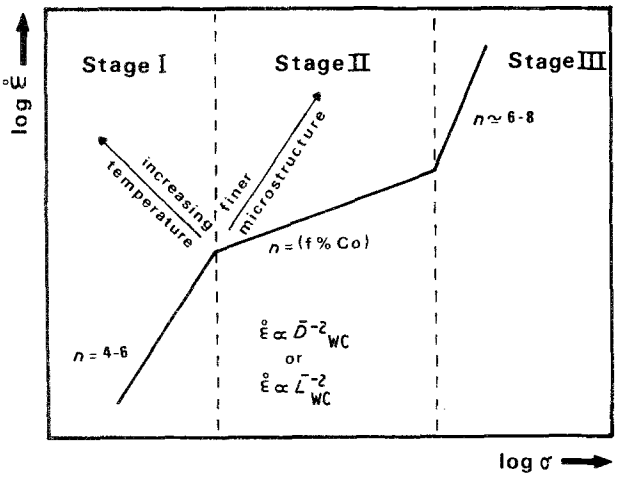

Figure 22 Schematization of the steady state creep rate domains and influence of tests and material parameters.

for low and high stresses the macroscopic creep rate of the material is governed by the majority phase. At an intermediate stress level the effective stress exponent $n = \partial \ln \dot{\varepsilon} / \partial \ln \sigma$ is a function of the constitutive creep laws and of the volume fractions of the phases.

In the discussion of the results, we excluded, on the basis of the stress and activation energy values, the idea that cobalt has a governing role in the creep process. The two phases to be considered are thus the isolated carbide crystals and the aggregates. However we can only speculate qualitatively on the relative amount of each. It needs basic assumptions on the formation of coincidence grain boundaries during the liquid phase sintering process which is not well known. We can only assume that the relative number of coincidence boundaries is an increasing function of the cobalt volume ratio.

This may be justified as follows. Since the liquid phase sintering involves a dissolution-reprecipitation process, the higher the cobalt volume ratio, the more space is available to allow the carbide crystals to reorientate and form the low energy coincidence grain boundaries. Furthermore, in view of Fig. 7, we can assume that centres of recrystallization will form, explaining thus the presence of carbide aggregates and of cobalt centres (large areas with ramifications). The values of the stress exponent can thus be written qualitatively as

$$n = f\left(\frac{Nc}{Ng + Nc}\right) \tag{5}$$

where Nc is the number of coincidence grain boundaries, and Ng the number of general grain boundaries.

Up to now the cobalt phase has been excluded as having a governing role in the creep process. It can however be assumed that cobalt contributes at least to the continuity of stress and that it may avoid

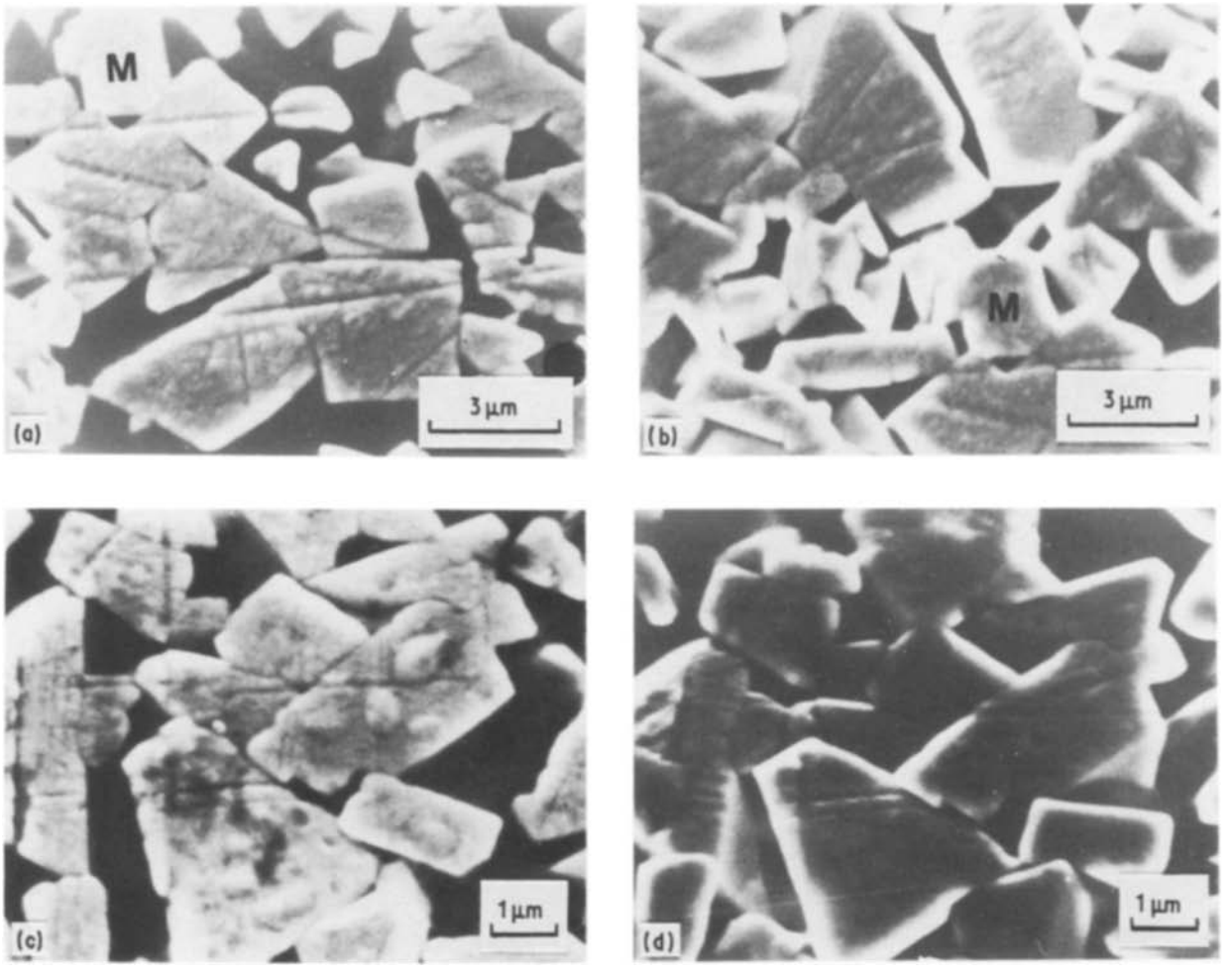

Figure 23 MEB images of a deformed WC–Co alloys for two deformation states. Non occurrence (a–b) or occurrence (c–d) of grain boundary sliding in the same sample ($\bar{D}_{WC}$ = 2.2 µm; 37 vol % Co) after different amounts of deformation: same area for (a) and (b) at 5% and 20% of deformation, another area for (c) and (d) at 5% and 10% of deformation, respectively.

cavitation. It would also be dangerous to state, without experimental verification, that replacing the cobalt by another binder would have no effect. Cobalt is present as a continuous or discontinuous [26] film in the general grain boundaries which act in the present case as perfect sinks. The wettability of WC by cobalt is very high and low energy phase-boundaries are formed. This may not be the case with other binders and the grain boundary sliding mechanism may thus be affected.

6. Conclusion

With the help of microstructural, analytical and transmission electron microscope investigations we have shown that the high temperature creep of tungsten carbide–cobalt alloys is governed by the deformation of the carbide phase. This phase forms either a skeleton or interlinked aggregates or chains over the whole domain of cobalt volume ratio investigated. A microstructural model was proposed to describe the material as three phased.

Further investigations on the microstructure and on the influence of different binders are necessary to refine this model and account for the influence of the binder volume ratio on the stress exponent where grain boundary sliding of the carbide crystals is present.

Acknowledgements

We would like to thank M. J.Y. Laval, Laboratoire d'étude et de synthèse des microstructures, ERA 912, CNRS-ESPCI for the STEM analysis. Part of this work has been performed under contract ATP-CNRS 91.81.80 and under ISMRa (CAEN) and CEN-SCK (MOL) association.

References

1. J. GURLAND and P. BARDZIL, *Trans. AIME* **203** (1955) 311.
2. M. NAKAMURA and J. GURLAND, *Met. Trans.* **11A** (1980) 141.
3. F. OSTERSTOCK, "Fracture mechanics of ceramics", vol. 6 (Plenum, New York, 1983) pp. 243–254.
4. J. S. SMITH and J. D. WOOD, *Acta Metall.* **16** (1968) 1219.
5. S. R. SCHENK, R. J. GOTTSCHALL and W. S. WILLIAMS, *Mater. Sci. Eng.* **33** (1978) 229.
6. F. OSTERSTOCK, "Science of hard materials", in Proceedings of the International Conference on the Science of Hard Materials, 1981, Jackson Lake Lodge, Wyoming, USA. Edited by R. K. Viswanadham, D. J. Rowcliffe and J. Gurland (Plenum, 1983) pp. 671–687.
7. G. ALTMEYER and O. JUNG, *Z. Metallkde* **52** (1961) 576.
8. W. DAWIHL and G. ALTMEYER, *ibid.* **54** (1963) 645.
9. M. K. MAL, PhD thesis, University of Sarreland, FRG, 1964.
10. J. BRATSPIES, PhD thesis, Lehigh University, USA, 1969.
11. F. UEDA, H. DOI, F. FUJIWARA, H. MASATOMI and Y. OOSAWA, *Trans. Jpn. Inst. Metals* **16** (1975) 591.
12. S. HAGEGE, PhD thesis, University of Caen, France, 1979.
13. S. HAGEGE, G. NOUET and P. DELAVIGNETTE, *Phys. Stat. Solidi* (a) **61** (1980) 97.
14. V. JAYARAM and R. SINCLAIR, *J. Amer. Ceram. Soc.* **66** (1983) C137.
15. T. WATANABE, M. YAMADA, S. SHIMA and K. KARASHIMA, *Phil. Mag.* **A40**, (1979) 667.
16. M. RUHLE, D.G.M., Tagung, Plenary Conference, Stuttgart, FRG, May 1985.
17. S. HAGEGE, J. VICENS, G. NOUET and P. DELAVIGNETTE, *Phys. Stat. Solidi.* (a) **61** (1980) 675.
18. M. K. HIBBS and R. SINCLAIR, *Acta Met.* **29** (1981) 1645.
19. R. M. GREENWOOD, M. H. LORETTO and R. SMALLMAN, *ibid.* **30** (1982) 1193.
20 R. J. GOTTSCHALL, W. S. WILLIAMS and I. D. WARD, *Phil. Mag.* **41** (1980) 1.
21. M. K. HIBBS, R. SINCLAIR and D. J. ROWCLIFFE, *Acta Met.* **32** (1984) 941.
22. R. K. VISWANADHAM, T. S. SUN, E. F. DRAKE and J. A. PECK, *J. Mater Sci.* **16** (1981) 1029.
23. C. LEA and B. ROEBUCK, *Met. Sci.* **15** (1981) 262.
24. J. L. CHERMANT and F. OSTERSTOCK, in Proceedings on the International Conference on the Science of Hard Materials, 1981, Jackson Lake Lodge, Wyoming, USA, edited by R. K. Viswanadham, D. J. Rowcliffe and J. Gurland (Plenum, 1983) pp. 615–629.
25. N. K. SHARMA, I. D. WARD, H. L. FRASERS and W. S. WILLIAMS, *J. Amer. Ceram. Soc.* **63** (1980) 194.
26. K. M. FRIEDERICH, *Met. Sci.* **17** (1983) 456.
27. J. Y. LAVAL, J. VICENS and G. NOUET, *J. Phys.* **45** (1984) 695.
28. J. L. CHERMANT, G. LECLERC and B. L. MORDIKE, *Z. Metallkde* **71** (1980) 465.
29. S. LAY, PhD thesis, University of Caen, France, 1985.
30. S. LAY, P. DELAVIGNETTE and J. VICENS, *Phys. Stat. Solidi* (a) **90** (1985) 53.
31. P. FELTHAM and T. A. MYERS, *Phil. Mag.* **8** (1963) 206.
32. T. SRITHARAM and H. JONES, *Acta Metall.* **27** (1979) 1293.
33. L. P. BUSHMER and P. H. CRAYTON, *J. Mater Sci.* **6** (1971) 981.
34. A. BISCONDI, *J. Phys.* **43 C6** (1982) 293.
35. F. W. CROSSMAN and M. F. ASHBY, *Acta Met.* **23** (1975) 425.
36. I. W. CHEN and A. S. ARGON, *ibid.* **27** (1979) 749.
37. *Idem, ibid.* **27** (1979) 785.
38. E. KRONER, *Z. Physik* **151** (1958) 504.
39. R. HILL, *J. Mech. Phys. Solids* **13** (1965) 213.
40. J. D. ESHELBY, *Proc. Roy. Soc.* **A241** (1957) 376.
41. M. J. MURRAY, D. C. SMITH, *J. Mater Sci.* **8** (1978) 1706.

Received 28 April
and accepted 13 August 1986